

pubs.acs.org/JACS Article

Structural Diversity in Dimension-Controlled Assemblies of Tetrahedral Gold Nanocrystals

Yi Wang, Jun Chen, Yaxu Zhong, Soojin Jeong, Ruipeng Li, and Xingchen Ye*



Cite This: J. Am. Chem. Soc. 2022, 144, 13538-13546



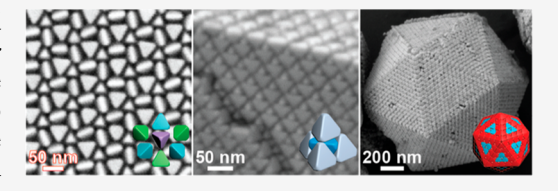
ACCESS

III Metrics & More

Article Recommendations

Supporting Information

ABSTRACT: Polyhedron packings have fascinated humans for centuries and continue to inspire scientists of modern disciplines. Despite extensive computer simulations and a handful of experimental investigations, understanding of the phase behaviors of synthetic tetrahedra has remained fragmentary largely due to the lack of tetrahedral building blocks with tunable size and versatile surface chemistry. Here, we report the remarkable richness of and complexity in dimension-controlled assemblies of gold nanotetrahedra. By tailoring nano-



crystal interactions from long-range repulsive to hard-particle-like or to systems with short-ranged directional attractions through control of surface ligands and assembly conditions, nearly a dozen of two-dimensional and three-dimensional superstructures including the cubic diamond and hexagonal diamond polymorphs are selectively assembled. We further demonstrate multiply twinned icosahedral supracrystals by drying aqueous gold nanotetrahedra on a hydrophobic substrate. This study expands the toolbox of the superstructure by design using tetrahedral building blocks and could spur future computational and experimental work on self-assembly and phase behavior of anisotropic colloidal particles with tunable interactions.

INTRODUCTION

Polyhedron packings have intrigued humans since ancient times and underpin a wide range of phenomena and applications in modern science and technology. 1-3 Selfassembly of polyhedral building blocks into complex superstructures, which is usually dictated by free-energy minimization, goes far beyond a packing problem and can be sensitive to the object shape, size, composition, surface functionality, and assembly condition.⁴⁻⁹ Assemblies of polyhedral shapes have been experimentally explored on many length scales including, among others, macroscopic dices, ¹⁰ micron-sized colloids, ^{11–13} nanocrystals, ^{4–7,9} metal–organic frameworks, ¹⁴ DNA origami cages, ¹⁵ and giant organic molecules. ¹⁶ Recent advances in nanocrystal synthesis and surface modifications provide precise control over particle shape and interaction, which have enabled studies of rich phase behaviors of polyhedral nanocrystals.^{1/-} Despite extensive research, the tetrahedron, the simplest Platonic solid and one of the most intriguing noncentrosymmetric shapes, remains much less explored in nanocrystal assemblies largely because of the inaccessibility to size-tunable nanotetrahedra with versatile surface chemistry. A tetrahedron is a basic structural unit in many atomic and molecular systems such as carbon diamond, silicon, water ice,² and Frank-Kasper phases.²⁸ Computer simulations by Glotzer and colleagues demonstrated that regular tetrahedra assemble into an entropically favored dodecagonal quasicrystal, whereas cubic diamond, β -tin, and high-pressure lithium structures can be attained by assembling tetrahedra with varying degrees of vertex and edge truncations. ^{29,30} Experimentally, Talapin and co-workers identified a low-density phase formed by zincblende CdSe nanotetrahedra.³¹ Chen and co-workers reported

several superstructures composed of wurtzite CdSe–CdS core—shell truncated nanotetrahedra including body-centered cubic, quasicrystal-approximant, and decagonal quasicrystalline phases. The gap between theoretical analyses or computational predictions and experimental outcomes highlights the importance and lack of control of particle interactions in colloidal nanotetrahedra.

Here, we report the synthesis of size-tunable gold nanotetrahedra and their self-assembly into ordered superstructures. By tuning nanocrystal interactions from long-range repulsive to hard-particle-like or to systems with short-ranged directional attractions through control of surface chemistry and assembly conditions, we obtained a rich diversity of dimensioncontrolled assemblies. These include six two-dimensional (2D) superstructures with distinct wallpaper symmetries, several three-dimensional (3D) superstructures including the cubic diamond and hexagonal diamond polymorphs, and discrete supracrystals of multiply twinned icosahedral- and hexagonal-plate shapes. This study not only uncovers the remarkable richness and complexity of nanotetrahedron assemblies but could also stimulate future computational studies that go beyond hard polyhedra by incorporating enthalpic contributions.

Received: March 24, 2022 Published: July 21, 2022





EXPERIMENTAL SECTION

Synthesis of Gold Tetrahedra. Gold tetrahedra were synthesized based on a previously reported method with modifications. 34 In the first step, ~10 nm gold spheres were prepared. Typically, 5 mL of 0.5 mM HAuCl₄ was mixed with 5 mL of 200 mM cetyltrimethylammonium bromide (CTAB) in a 20 mL scintillation vial at 28 °C. Then, 0.6 mL of freshly prepared 10 mM NaBH₄ was quickly injected under vigorous stirring (~1500 rpm). After stirring for 30 s, the mixture was left undisturbed at 28 °C for 4.5 h. Separately, a growth solution was prepared by mixing 80 mL of 200 mM cetyltrimethylammonium chloride (CTAC), 80 mL of 0.5 mM HAuCl₄, and 60 mL of 100 mM L-ascorbic acid solutions. After the growth solution turned colorless, 4 mL of the seed solution was added, and the resulting solution was gently stirred for 1 h at 28 °C. Gold spheres were purified via two rounds of centrifugation at 8500 rpm for 30 min, each time re-dispersed into 20 mM CTAC (aq). The gold sphere solution was finally brought to an optical density (O.D.) of 2.0 at an extinction peak wavelength of ~521 nm using 20 mM CTAC (aq) (Figure S1).

In the second step, gold tetrahedra were synthesized by using gold spheres as seeds. Typically, to synthesize 49 nm tetrahedra, 3 mmol (0.96 g) CTAC, 1 mmol (0.364 g) CTAB, and 40 mL of H₂O were mixed under stirring at 30 °C. Once CTAC and CTAB were fully dissolved, 20 mL of 200 mM L-ascorbic acid (aq) and 2 mL of the above-mentioned gold sphere solution were added consecutively to the mixture. Next, 20 mL of 2.5 mM HAuCl₄ solution was added dropwise by using a syringe pump (4.8 mL/h) under gentle stirring at 29 °C. Afterward, the reaction mixture was left undisturbed at 29 °C for another 10 min. Gold tetrahedra were purified via three rounds of centrifugation at 7000 rpm for 15 min, each time re-dispersed into 20 mM CTAC (aq). Finally, gold tetrahedra were dispersed into ~1 mL of 20 mM CTAC. The size of gold tetrahedra was tuned by changing the volume of HAuCl₄ solution used in the second step, as detailed in Table S1.

Purification of Gold Tetrahedra by Using Depletion Attraction. Typically, to purify 49 nm gold tetrahedra via depletion attraction, 0.5 mL of the tetrahedron solution was added to a 15 mL centrifugation tube. Next, 4.5 mL of 350 mM CTAC was added to provide the depletion attraction which favors face-to-face contact between the flat faces of tetrahedra while excluding spherical or illshaped impurities. This mixture was left undisturbed overnight to allow the flocculation and sedimentation of tetrahedra. Afterward, the supernatant was carefully removed with a pipette, and the pellets at the bottom of the tube were further rinsed with 100 μ L of 350 mM CTAC twice to remove any weakly adsorbed impurity particles. The pellets were dispersed in 1 mL of 20 mM CTAC and purified via one round of centrifugation at 3500 rpm for 20 min. The pellets were finally re-dispersed in 0.5 mL of 20 mM CTAC for later use. Different concentrations of CTAC were employed to purify gold tetrahedra of different sizes, as detailed in Table S1.

Synthesis of Pentaethylenehexamine-Terminated Polystyrene. Details regarding the synthesis of pentaethylenehexamineterminated polystyrene (PS-PEHA) have been described in our previous publications.^{35,36} Further details on material synthesis and characterization are provided in the Supporting Information (SI).

Functionalization of Gold Tetrahedra with PS-PEHA and Self-Assembly of PS-Grafted Tetrahedra. To attain adequate surface passivation, highly concentrated gold tetrahedron solution with a low CTAC content and excess PS-PEHA ligands was used during ligand-exchange reactions. Typically, 2 µL of the nanocrystal solution (O.D. = 500) was added to a separately prepared tetrahydrofuran (THF) solution of PS-PEHA under vortexing. After sonicating for ~10 s, this mixture was left undisturbed for 24 h. The concentration and volume of PS-PEHA solutions used for ligand exchange were molecular-weight-dependent, as detailed in Table S4.

To prepare 2D gold tetrahedron superstructures, 20 μ L of toluene solution of PS-grafted tetrahedra was drop-casted onto the surface of ethylene glycol (EG) inside a Teflon well (1.5 \times 1.5 \times 1 cm³). The Teflon well was quickly covered with a glass slide to slow down solvent evaporation. To fabricate 3D superstructures, 20 µL of toluene solution of PS-grafted gold tetrahedra was added onto a

copper transmission electron microscopy (TEM) grid which was placed inside a titling glass vial (ca. 25° with respect to the horizontal) (Figure S2). The glass vial was loosely capped to allow slow solvent evaporation under ambient conditions.

Self-Assembly of CTAC-Capped Gold Tetrahedra. Gold tetrahedron solutions of varying CTAC concentrations were prepared by diluting the tetrahedron stock solution (in 20 mM CTAC) with water or by adding a certain amount of 200 mM CTAC solution. The nanocrystal concentration was kept at O.D. = 50 for each deposition. To fabricate 3D superstructures, 20 µL of CTAC-capped gold tetrahedron solution was drop-casted onto a Si substrate, which was left to dry in open air (typically ~ 1.5 h).

Functionalization of Gold Tetrahedra with 11-Mercaptoundecanoic Acid (MUA) and Self-Assembly of MUA-Capped Gold Tetrahedra. Gold tetrahedra were functionalized with MUA using a previously reported method with modifications. 37 To fabricate 3D superstructures, 10 μ L of MUA-capped gold tetrahedra was mixed with 10 μ L of water, and the resulting solution was drop-casted onto a Si substrate. The droplet was left to dry in open air for ~2 h. The same deposition procedure was used to fabricate discrete supracrystals, except that a PS brush-modified Si substrate was used.

RESULTS AND DISCUSSION

Gold nanotetrahedra were synthesized based on a seedmediated growth method reported by Xia and co-workers with modifications.³⁴ The crude products were purified using CTAC micelles as depletants to improve sample uniformity (Figure S3). The tetrahedral shape was confirmed by the gradual increase in brightness toward the nanocrystal center observed from the high-angle annular dark-field scanning TEM (HAADF-STEM) image (Figure 1a,b). The edge length (l_1) of gold tetrahedra can be tuned from 35 to 80 nm by increasing the molar ratio of gold precursor to nanocrystal seeds (Figure 1c-e and Table S1). The degree of truncation, defined as 1 minus the ratio between measured (l_2) and extrapolated (l_1) triangular edge lengths from TEM images, varies between 0.32 and 0.40 (Figure S4). A high-resolution TEM image and coherent nano-area electron diffraction (CNED) pattern reveal that each gold tetrahedron is singlecrystalline and bound by {111}_{NC} crystal planes (Figure 1f,g). In this work, we denote the crystallographic planes of the nanocrystal and the superlattice with subscripts "NC" and "SL", respectively. The major plasmonic peak red-shifts from 564 to 594 nm with increasing tetrahedron size (Figure 1h). The gradual emergence of a small shoulder peak centered at ~525 nm for larger tetrahedra likely results from the hybridization between quadrupole and dipole plasmonic vertex modes supported by gold tetrahedra.³¹

To form 2D superstructures, a toluene solution of polymergrafted gold tetrahedra was allowed to dry on top of immiscible EG (Figure 2a). Narrowly dispersed PS-PEHA ligands with number-average molecular weights (M_n) ranging from 1.6 to 39 kDa were synthesized and grafted onto gold tetrahedra through ligand exchange (Figures S5 and S6 and Tables S2-S4).35,36 We found that the ratio of ligand length to nanotetrahedron edge length (or equivalently, tetrahedron softness)⁶ is the key parameter to generate the phase diagram, which includes six distinct 2D superlattices (Figure 2b). Large tetrahedra ($l_1 = 57$ nm) grafted with the shortest ligands ($M_p =$ 1.6 kDa) assemble into a triangular lattice. The unit cell consists of two tetrahedra in opposite face-up and vertex-up orientations (Figures 2d and S7a). Each tetrahedron contacts three neighboring tetrahedra in a face-to-face antiparallel arrangement (Figures S8 and S9). A slight increase in tetrahedron softness induces lattice deformation parallel to

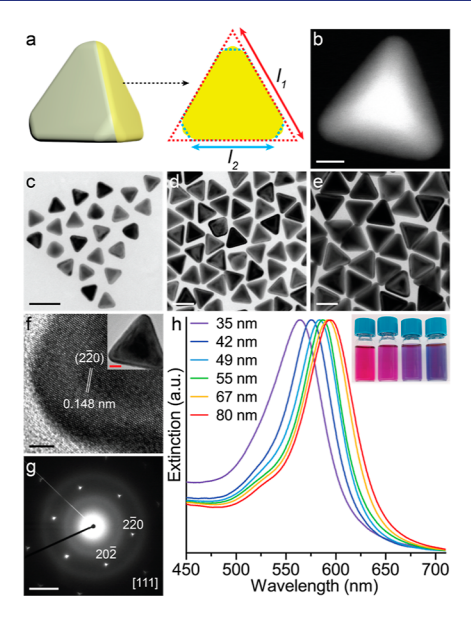


Figure 1. Synthesis and characterization of gold tetrahedra. (a) Schematic of a truncated gold tetrahedron and the projection view perpendicular to one of the four $\{111\}_{NC}$ surface facets. The degree of truncation, t, is defined as 1 minus the ratio of the measured edge length (l_2) to the extrapolated edge length (l_1) . (b) HAADF-STEM image of a single gold tetrahedron. (c-e) TEM images of gold tetrahedra with mean edge lengths of 35 (c), 57 (d), and 80 (e) nm. (f) HRTEM images of a single gold tetrahedron (inset) and a magnified view of one tetrahedron vertex (main image). (g) CNED pattern of the gold tetrahedron shown in (f). (h) UV-vis extinction spectra of gold tetrahedra with mean edge lengths ranging from 35 to 80 nm. The inset shows a photograph of gold tetrahedron solutions with mean edge lengths of (from left to right) 35, 44, 57, and 80 nm. Scale bars: (b) 10 nm, (c-e) 50 nm, (f) 2 nm, (f, inset) 10 nm, and (g) 5 nm⁻¹.

tetrahedron edges, resulting in a centered rectangular lattice whose unit cell is composed of two face-up and two vertex-up tetrahedra (Figures 2e and S7b). Besides face-to-face contacts between antiparallel-aligned neighbors, new contact modes emerge including edge-to-edge (vertex-to-vertex) contacts between oppositely (samely) oriented tetrahedra. A further increase in tetrahedron softness produces a rectangular lattice with rows of tetrahedra alternating between face-up and vertex-up orientations (Figures 2f and S7c,d). Here, tetrahedra of the same row engage in vertex-edge contacts with two neighbors, whereas tetrahedra from adjacent rows have both face-to-face and edge-to-edge contacts.

As particle softness continues to increase, edge-up tetrahedra emerge in 2D superstructures. An exotic centered rectangular lattice characterized by plentiful edge-to-edge contacts among neighbors was obtained first. Its unit cell has eight tetrahedra adopting three orientations: two face-up, two vertex-up, and four edge-up (Figures 2g and S7e). With even longer ligands, all tetrahedra assume the edge-up orientation. The resultant herringbone lattice (two tetrahedra per unit cell) features alternating rows of orthogonally oriented tetrahedra with adjacent rows offset by half a unit cell width (Figure 2c,h). Notably, edge-to-edge contacts dominate this herringbone structure, whereas face-to-face contact is suppressed. Eventually, with sufficiently long ligands, individual tetrahedra lose the orientational order and preferred contact modes with neighbors, which gives rise to a hexagonal plastic phase (Figures 2i and S10).

The diverse nanotetrahedron superstructures attained by changing the ratio of ligand length to tetrahedron edge length are unprecedented for single-component 2D nanocrystal assemblies. We attribute the rich self-assembly behaviors to the non-centrosymmetric tetrahedral shape for which the nanocrystal orientation, contact mode, and lattice symmetry have different dependencies on nanocrystal softness. First, multiple tetrahedron orientations (i.e., face-up, vertex-up, and edge-up) can coexist in a superstructure. By contrast, centrosymmetric polyhedra tend to adopt the same orientation in ordered assemblies.² Second, preferred contact modes between nanotetrahedra are greatly enriched by tuning particle softness. At a low degree of softness (Figure 2d-f), tetrahedra assemble into dense-packing phases by maximizing face-to-face contacts. Increasing ligand length causes an effective rounding of the tetrahedral shape and accompanying lattice symmetry transitions. Such in-plane lattice distortion without particle reorientation stems from a collective response to changing effective shapes of nanocrystals, which has been documented in experimental and computational studies of phase behavior of rounded polyhedra. ^{12,36,39} At a high degree of softness (Figure 2g-i), pronounced shape rounding reduces the preference for face-to-face contacts. 40,41 Also, edge-to-edge contacts can better promote ligand interdigitation and superstructure densification in comparison to face-to-face contacts because ligands grafted at regions of high local curvature can tilt away more easily from the axis of contact to lower the osmotic repulsion between opposing polymer brushes.^{31,36} Taken together, our results indicate that the preference for face-toface contacts among gold nanotetrahedra diminishes gradually with increasing particle softness, which ultimately triggers the switch to the "edge-up" tetrahedron orientation that facilitates edge-to-edge contacts in 2D superstructures.

To form 3D superstructures, a sessile droplet of gold tetrahedron aqueous solution was dried on a hydrophilic Si substrate (Figure 3a). As water evaporates, nanocrystals concentrate at the drying front due to capillary flow, 42 forming a dense, roughly 20 μ m-wide ring-like deposit. The Si substrate was cracked to reveal the internal structure of 3D assemblies. Cross-sectional scanning electron microscopy (SEM) images show that at low CTAC concentrations (≤ 0.1 mM), three distinct superstructures are formed across the deposits. A monoclinic phase forms at the outermost region (Figures 3b and S11). A top-view SEM image reveals that the superstructure surface adopts a centered rectangular packing with tetrahedra alternating between face-up and vertex-up orientations. Based on cross-sectional SEM imaging, the interior of the lattice consists of columns of samely oriented tetrahedra in face-to-vertex contact normal to the top surface, whereas faceto-face contacts predominate within layers parallel to the top surface (Figure 3c,d). In the middle region of the deposit, we identified the cubic diamond phase featuring three adjacent {111}_{SL} cleavage planes. Each tetrahedron is surrounded by four antiparallel face-to-face aligned neighbors (Figures 3e-g and S12). In the innermost deposit area, the hexagonal diamond phase was identified (Figures 3h-j and S13). The cubic diamond and hexagonal diamond polymorphs are both composed of triangularly packed tetrahedron layers, except that fully aligned tetrahedron dimers are formed between neighboring layers in the hexagonal diamond structure.

The coexistence and spatial distribution pattern of tetrahedron superstructures derived from drying-mediated assembly suggest that the local CTAC concentration could

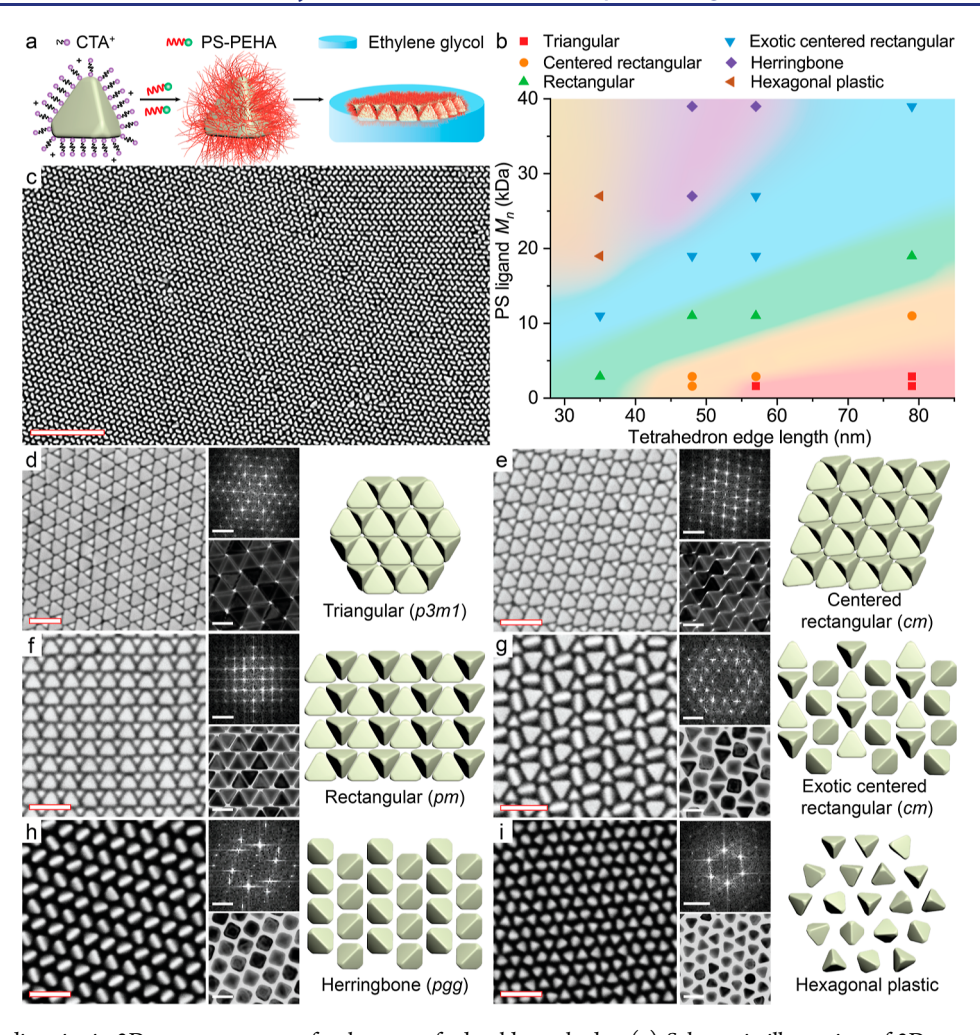


Figure 2. Structural diversity in 2D superstructures of polymer-grafted gold tetrahedra. (a) Schematic illustration of 2D superstructure formation through interfacial assembly. (b) Experimental phase diagram of 2D superstructures as a function of tetrahedron edge length and the molecular weight of polystyrene ligands. (c) Low-magnification SEM image of the herringbone superstructure. (d–i) SEM images (left), corresponding FFT patterns (middle top), TEM images (middle bottom), and structure models (right) of 2D superstructures exhibiting triangular (M_n = 1.6 kDa, l_1 = 57 nm) (d), centered rectangular (M_n = 2.9 kDa, l_1 = 48 nm) (e), rectangular (M_n = 11 kDa, l_1 = 48 nm) (f), exotic centered rectangular (M_n = 19 kDa, l_1 = 48 nm) (g), herringbone (M_n = 39 kDa, l_1 = 48 nm) (h), and hexagonal plastic (M_n = 27 kDa, l_1 = 35 nm) (i) packing symmetries. The plane group symmetry of each structure is denoted by notations in parentheses. Scale bars: (c) 500 nm, (d–i) SEM images 100 nm, (d–f,i) FFT patterns 0.05 nm⁻¹, (g,h) FFT patterns 0.025 nm⁻¹, and (d–i) TEM images 50 nm.

play a central role in determining which phases are favored. Therefore, we varied the starting CTAC concentration of the droplet, and the results are summarized in a phase diagram (Figure 4a,b). At intermediate CTAC concentrations (0.1–2 mM), cubic diamond and hexagonal diamond superstructures are formed in the outer and inner areas of the deposit, respectively. At high CTAC concentrations (≥ 2 mM), only the hexagonal diamond phase can be obtained.

The formation of the cubic diamond lattice suggests that the interactions among gold nanotetrahedra are nearly hard-particle-like, as supported by computer simulations of self-assembling truncated hard tetrahedra. At low CTAC concentrations (\leq 0.1 mM), the interactions become long-range repulsive due to the large Debye lengths (comparable to nanotetrahedron dimensions) (Figure S14). We postulate that the monoclinic phase is favored for nanotetrahedra characterized by soft interaction potentials. This argument is further supported by the formation of the same structure from PS-grafted gold nanotetrahedra (Figure S15) and a previous study on alkyl-capped CdSe nanotetrahedra of \sim 10 nm edge

length.³¹ At high CTAC concentrations exceeding its critical micelle concentration (cmc, 1.3 mM), 43 the Debye length is considerably shorter than the edge length of tetrahedra (Figure S14), while depletion attractions caused by CTAC micelles become significant. 44,45 To shed light on the structural transition from cubic diamond to hexagonal diamond, we calculated the pairwise interaction energies for parallel and antiparallel face-to-face aligned gold nanotetrahedra taking into account van der Waals, electrostatic, and depletion interactions (Figure 4c and Supporting Information Section S5). The difference in minimum energy between the two configurations increases with the CTAC concentration (Figure S16), suggesting that the hexagonal diamond structure becomes more favorable at higher CTAC concentrations (above cmc). Further evidence supporting the importance of depletion attractions in stabilizing hexagonal diamond is that MUAcapped gold tetrahedra self-assemble into predominantly the cubic diamond lattice (Figure S17). Pairwise interaction energy calculations considering only van der Waals attraction and electrostatic repulsion indicate that the differences in

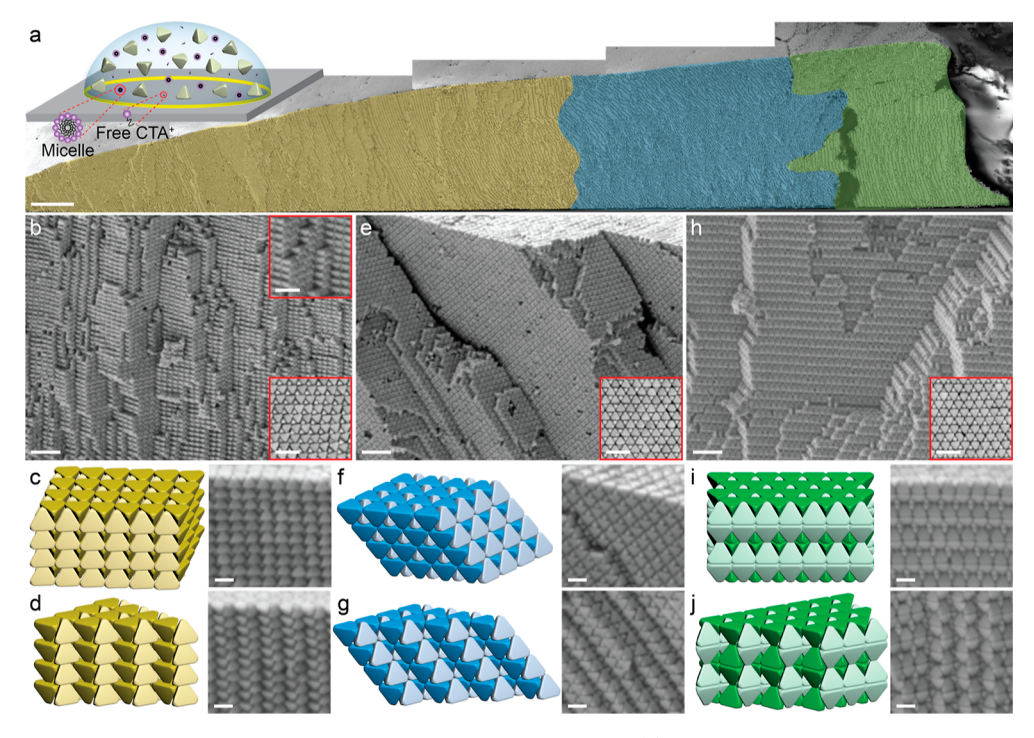


Figure 3. Structural diversity in 3D superstructures of CTAC-capped gold tetrahedra. (a) Ultralow-magnification cross-sectional SEM image of 3D superstructures obtained by drying-mediated assembly at low CTAC concentration on a Si substrate. Three regions of distinct superstructures, namely, monoclinic (yellow), cubic diamond (blue), and hexagonal diamond (green) lattices, are color-coded accordingly. The top-left inset shows the schematic of an evaporating aqueous solution droplet of gold tetrahedra. (b-j) Low-magnification cross-sectional SEM images (b,e,h), structure models, and corresponding high-magnification cross-sectional SEM images of monoclinic (b-d), cubic diamond (e-g), and hexagonal diamond superstructures (h-j). The upper right inset of (b) is a high-magnification cross-sectional SEM image, and the bottom right insets of (b,e,h) are representative top-view SEM images. Scale bars: (a) 1 μ m, (b,e,h) main SEM images 200 nm, (b,e,h) insets 100 nm, and (c,d,f,g,i,j) 50 nm.

minimum energy between two configurations are insignificant over a wide range of salt concentrations, thereby disfavoring the structural transition from cubic diamond to hexagonal diamond (Figure \$18).

We further conducted simultaneous grazing-incidence smallangle and wide-angle X-ray scattering (GISAXS/GIWAXS) and transmission SAXS measurements on the 3D superstructures to deduce lattice symmetries and quantify lattice parameters. The monoclinic, cubic diamond, and hexagonal diamond superstructures were self-assembled from PS-grafted tetrahedra, MUA-capped tetrahedra, and CTAC-capped tetrahedra in the presence of depletants, respectively. The unit cells determined based on SEM images and X-ray scattering measurement results are shown in Figure 4d. The long-range translational and orientational ordering of the superlattices was confirmed by the SAXS and WAXS patterns, respectively (Figures 4e-i and S19 and S20). The GISAXS and transmission SAXS patterns of the monoclinic lattice are indexed to a $[001]_{SL}$ -oriented C2/m lattice with b/a = 0.83, c/a = 0.57, and $\alpha = \beta = \gamma = 90^{\circ}$ (Figures 4e,f and S19a,c,d). The absence of $\{100\}_{SL}$ and $\{010\}_{SL}$ indicates a C-centered lattice. The GISAXS pattern of the cubic diamond superstructure exhibits sharp diffraction peaks that can be indexed as a [111]_{SL}-oriented face-centered cubic (FCC) lattice (space group: $Fm\overline{3}m$, a=b=c, $\alpha=\beta=\gamma=90^{\circ}$). The appearance of $\{222\}_{SL}$ and $\{002\}_{SL}$ scattering spots which should be forbidden for the conventional cubic diamond lattice could have its origin in the anisotropic shape of the tetrahedral building blocks (Figure 4g). The GISAXS pattern of the hexagonal diamond superstructure is indexed as a [001]_{SL}-

oriented hexagonal lattice (space group: $P6_3/mmc$, a=b, c/a=1.48, $\alpha=\beta=90^\circ$, $\gamma=120^\circ$) (Figures 4h and S19b). The smaller c/a ratio compared with a c/a ratio of 1.63 for the conventional hexagonal diamond lattice indicates lattice contraction along the c-direction, which likely results from the depletion attraction between face-to-face parallelly aligned tetrahedra. Furthermore, the GIWAXS patterns of all superstructures are $[111]_{\rm NC}$ -oriented with the triangular faces parallel to the substrate (Figures 4i and S20), consistent with SEM imaging results.

We also investigated the formation of discrete supraparticles by drying an aqueous solution of MUA-capped gold nanotetrahedra on a hydrophobic PS-modified Si substrate in open air (Figure 5a). Contact line pinning and crystallization from the substrate are greatly suppressed due to the high contact angle of the droplet. Multiply twinned supracrystals were observed as the major product, among which ~15% adopted the icosahedral shape (Figure 5b-e). Icosahedral supraparticles consisting of 20 tetrahedral domains with equilateral triangular faces are formed with diameters ranging from 380 nm to 1.5 μ m (Figures 5c-e and S21). Five twin planes featuring tetrahedron dimers are evident when viewed along one of the fivefold symmetry axes (Figure 5f,g). The internal structure was revealed by examining defective areas of icosahedral supraparticles (Figure 5h): Each gold nanotetrahedron within the single-crystalline subdomains coordinates with four antiparallelly aligned neighbors, reminiscent of the cubic diamond lattice. All exposed surfaces of the icosahedra belong to the cubic diamond $\{111\}_{SL}$ plane family. Based on the postulated structural model, the supraparticles

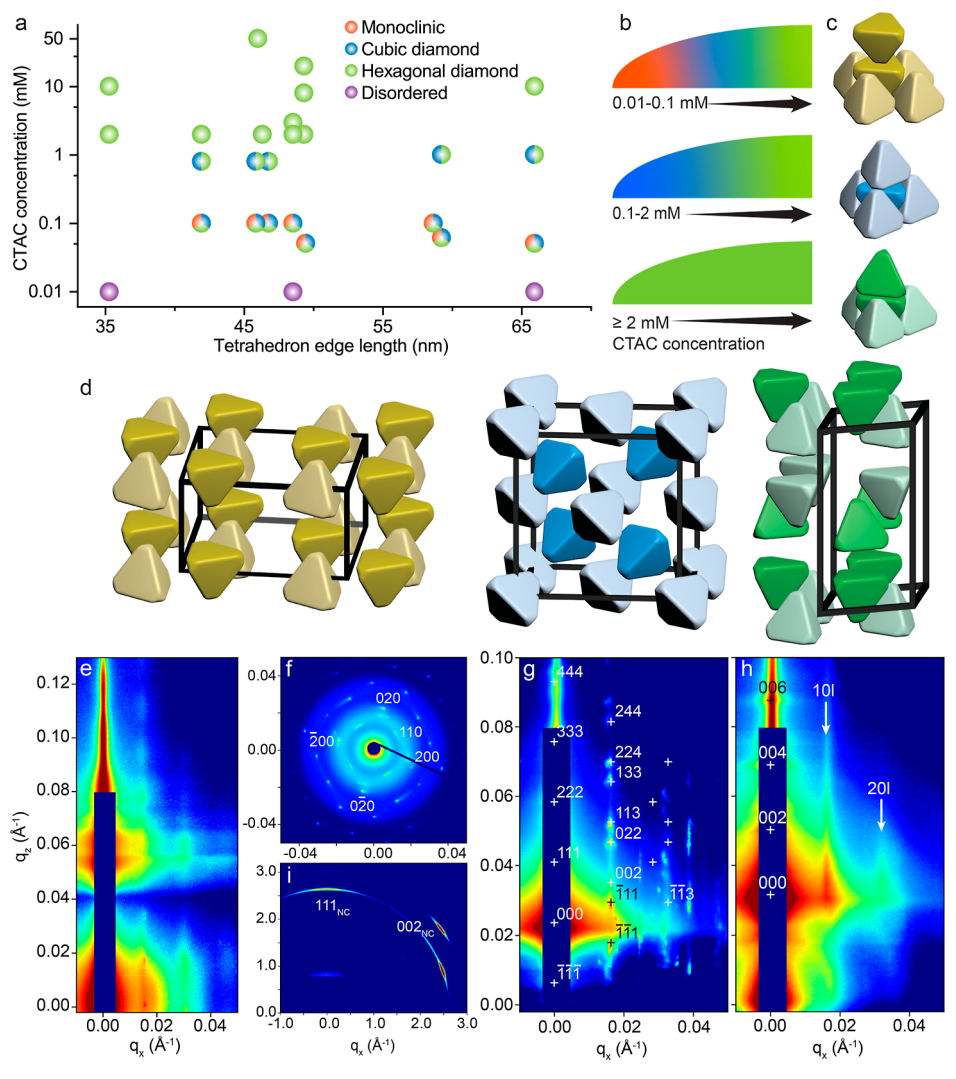


Figure 4. Experimental phase diagram and synchrotron X-ray scattering characterization results of 3D superstructures of gold tetrahedra. (a) Experimental phase diagram of 3D superstructures of gold tetrahedra as a function of the tetrahedron edge length and initial CTAC concentration. Those multi-color circles indicate a coexistence of multiple superstructures, while the areal fraction of the color does not reflect the relative proportions of different phases. (b) Schematic illustrations of an evaporating droplet of gold tetrahedron solution and the spatial locations of 3D superstructures with different initial CTAC concentrations (indicated below each graph). Experimentally observed spatial patterns of monoclinic (red), cubic diamond (blue), and hexagonal diamond (green) lattices are depicted. (c) Structure models showing the local coordination environment of tetrahedra. (From top to bottom) Face-to-vertex, antiparallel face-to-face, and parallel face-to-face alignments between two tetrahedra from neighboring layers are featured in the monoclinic, cubic diamond, and hexagonal diamond lattices, respectively. (d) Structure models of superstructure unit cells. (e,f) GISAXS pattern (e) and transmission SAXS pattern (f) of the monoclinic superstructure. (g—h) GISAXS patterns of the cubic diamond (g) and hexagonal diamond (h) superstructures. (i) GIWAXS pattern of the monoclinic superstructure.

are composed of around 1100 to 66,000 nanotetrahedra corresponding to a total of 9 to 41 shells. The incorporation of twin planes in the cubic diamond lattice may lower the total free energy of the supraparticle by maximizing the low-energy {111}_{SL} facets while keeping the surface-to-volume ratio to a minimum. An Notably, multiply twinned icosahedra have been observed in chemical vapor-deposited carbon diamond. The elastic strain inherent in multi-twinned structures can be relaxed by incorporating structural defects. For example, imperfect face-to-face alignment between tetrahedra at the twin boundaries has been observed for many icosahedral supraparticles. Other modes of strain relaxation such as lattice expansion may also be present and deserve further investigation. Dimples at the fivefold axes and reentrant grooves between adjacent {111}_{SL} facets were frequently

noticed (Figure S21), which could originate from kinetic faceting.⁴⁷

Hexagonal plate-shaped supracrystals are also formed, which are composed of layers of triangularly packed tetrahedra and random stacking faults along the thickness direction (Figures 5i,j and S22). The reentrant grooves on the sides can provide preferential sites for incoming nanotetrahedra resulting in the plate morphology. 48

CONCLUSIONS

In summary, we synthesized monodisperse gold nanotetrahedra with tunable edge length and studied their self-organization into diverse superlattices. A total of 11 distinct superstructures were obtained, 10 of which are realized experimentally for the first time with colloidal nanotetrahedra. Six 2D superstructures with distinct wallpaper symmetries were attained by varying

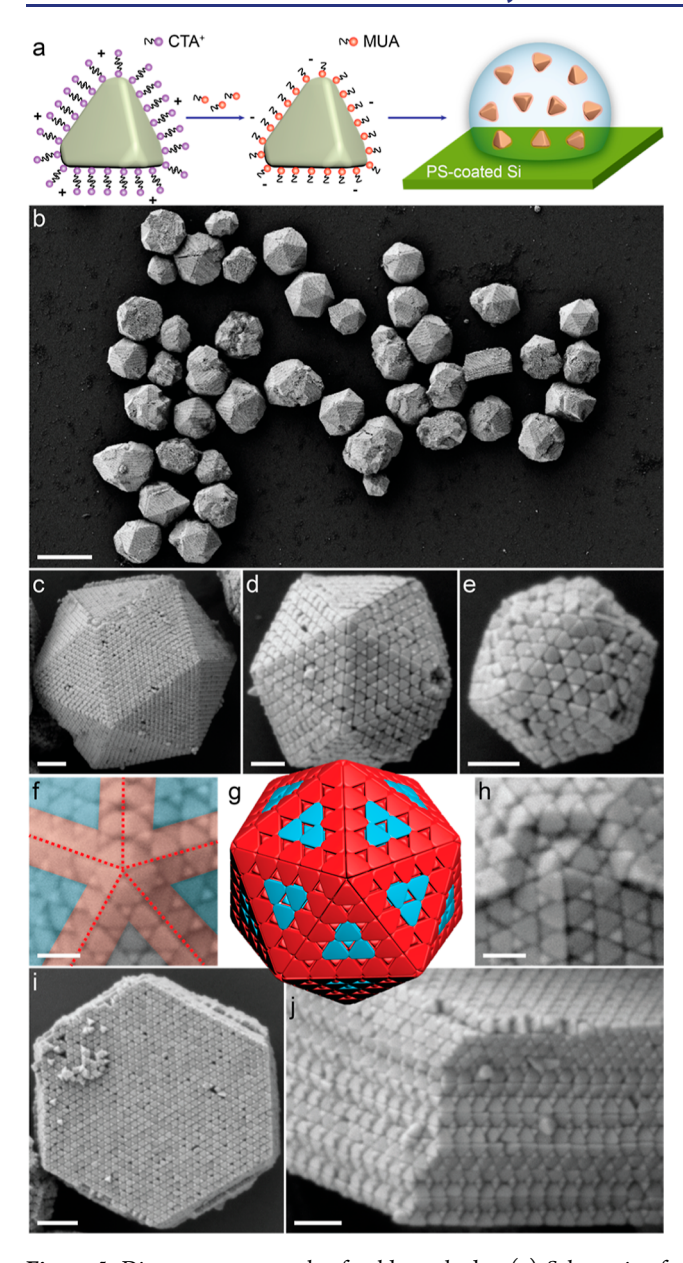


Figure 5. Discrete supracrystals of gold tetrahedra. (a) Schematic of preparation of MUA-capped gold tetrahedra through ligand exchange and formation of discrete supracrystals via drying-mediated assembly on a hydrophobic PS-coated Si substrate. (b) Low-magnification SEM image of discrete supracrystals. (c-e) SEM images of a single icosahedral supracrystal of gold tetrahedra with a supracrystal diameter of 1.4 µm (c), 660 nm (d), and 380 nm (e). (f-h) Highmagnification SEM images (f,h) and structure model (g) of icosahedral supracrystals viewed along the fivefold axis. The twin planes in (f) are indicated with red dashed lines. Individual icosahedral supracrystals are characterized by two distinct subregions: 20 tetrahedral domains (blue overlays) of the icosahedron each adopting the cubic diamond structure and twin planes (red overlays) featuring face-to-face parallelly aligned tetrahedra. (i,j) Top-view (i) and side-view (j) SEM images of a single hexagonal plate-shaped supracrystal characterized by randomly stacked layers of triangularly packed tetrahedra. Scale bars: (b) 2 μ m, (c,i) 200 nm, (d,e,j) 100 nm, and (f,h) 50 nm.

the ratio of polymeric ligand length to tetrahedron edge length. Moreover, nearly phase-pure monoclinic, cubic diamond, and hexagonal diamond 3D superstructures were achieved by assembling PS-grafted tetrahedra, MUA-capped tetrahedra,

and CTAC-capped tetrahedra in the presence of depletants, respectively. Lastly, discrete multiply twinned supraparticles of icosahedral and hexagonal-plate shapes were synthesized by drying aqueous solutions on hydrophobic substrates. The remarkable richness and complexity of nanotetrahedron assemblies uncovered here may spur future computational and experimental studies on the phase behavior of anisotropic nanocrystals with tunable interactions. Also, we anticipate that the availability of size-tunable, monodisperse gold nanotetrahedra will open up a host of new possibilities for research on plasmonics, optical metamaterials, surface-enhanced spectroscopies, and light-mediated energy conversions, among others.

ASSOCIATED CONTENT

Supporting Information

The Supporting Information is available free of charge at https://pubs.acs.org/doi/10.1021/jacs.2c03196.

Detailed experimental methods, pairwise interaction energy calculations, and material characterization; additional SEM images; supporting figures; and supporting tables (PDF)

AUTHOR INFORMATION

Corresponding Author

Xingchen Ye - Department of Chemistry, Indiana University, Bloomington, Indiana 47405, United States; oorcid.org/ 0000-0001-6851-2721; Email: xingye@indiana.edu

Authors

Yi Wang - Department of Chemistry, Indiana University, Bloomington, Indiana 47405, United States

Jun Chen - Department of Chemistry, Indiana University, Bloomington, Indiana 47405, United States; o orcid.org/ 0000-0001-9173-3450

Yaxu Zhong - Department of Chemistry, Indiana University, Bloomington, Indiana 47405, United States

Soojin Jeong – Department of Chemistry, Indiana University, Bloomington, Indiana 47405, United States

Ruipeng Li - National Synchrotron Light Source II, Brookhaven National Laboratory, Upton, New York 11973, United States

Complete contact information is available at: https://pubs.acs.org/10.1021/jacs.2c03196

Notes

The authors declare no competing financial interest.

ACKNOWLEDGMENTS

This work was supported by the U.S. National Science Foundation (NSF DMR-2102526). We thank the Indiana University Nanoscale Characterization Facility and the Electron Microscopy Center for access to instrumentation. This research used the Complex Materials Scattering beamline (11-BM) of the National Synchrotron Light Source II, a U.S. Department of Energy (DOE) office of the Science User Facility operated for the DOE Office of Science by Brookhaven National Laboratory under contract no. DE-SC0012704.

REFERENCES

- (1) Damasceno, P. F.; Engel, M.; Glotzer, S. C. Predictive self-assembly of polyhedra into complex structures. *Science* **2012**, 337, 453–457
- (2) Torquato, S.; Jiao, Y. Dense packings of the Platonic and Archimedean solids. *Nature* **2009**, *460*, 876–879.
- (3) Agarwal, U.; Escobedo, F. A. Mesophase behaviour of polyhedral particles. *Nat. Mater.* **2011**, *10*, 230–235.
- (4) Bishop, K. J.; Wilmer, C. E.; Soh, S.; Grzybowski, B. A. Nanoscale forces and their uses in self-assembly. *Small* **2009**, *5*, 1600–1630.
- (5) Batista, C. A.; Larson, R. G.; Kotov, N. A. Nonadditivity of nanoparticle interactions. *Science* **2015**, *350*, 1242477.
- (6) Boles, M. A.; Engel, M.; Talapin, D. V. Self-Assembly of colloidal nanocrystals: from intricate structures to functional materials. *Chem. Rev.* **2016**, *116*, 11220–11289.
- (7) Liu, J.; Huang, J.; Niu, W.; Tan, C.; Zhang, H. Unconventional-phase crystalline materials constructed from multiscale building blocks. *Chem. Rev.* **2021**, *121*, 5830–5888.
- (8) Dijkstra, M.; Luijten, E. From predictive modelling to machine learning and reverse engineering of colloidal self-assembly. *Nat. Mater.* **2021**, *20*, 762–773.
- (9) Li, Z.; Fan, Q.; Yin, Y. Colloidal self-assembly approaches to smart nanostructured materials. *Chem. Rev.* **2022**, *122*, 4976–5067.
- (10) Jaoshvili, A.; Esakia, A.; Porrati, M.; Chaikin, P. M. Experiments on the random packing of tetrahedral dice. *Phys. Rev. Lett.* **2010**, *104*, 185501–185504.
- (11) Zhao, K.; Bruinsma, R.; Mason, T. G. Entropic crystal-crystal transitions of Brownian squares. *Proc. Natl. Acad. Sci. U.S.A.* **2011**, 108, 2684–2687.
- (12) Rossi, L.; Soni, V.; Ashton, D. J.; Pine, D. J.; Philipse, A. P.; Chaikin, P. M.; Dijkstra, M.; Sacanna, S.; Irvine, W. T. Shape-sensitive crystallization in colloidal superball fluids. *Proc. Natl. Acad. Sci. U.S.A.* **2015**, *112*, 5286–5290.
- (13) He, M.; Gales, J. P.; Ducrot, E.; Gong, Z.; Yi, G. R.; Sacanna, S.; Pine, D. Colloidal diamond. *Nature* **2020**, *585*, 524–529.
- (14) Avci, C.; Imaz, I.; Carné-Sánchez, A.; Pariente, J. A.; Tasios, N.; Pérez-Carvajal, J.; Alonso, M. I.; Blanco, A.; Dijkstra, M.; López, C.; Maspoch, D. Self-assembly of polyhedral metal-organic framework particles into three-dimensional ordered superstructures. *Nat. Chem.* **2017**, *10*, 78–84.
- (15) Liu, W.; Tagawa, M.; Xin, H. L.; Wang, T.; Emamy, H.; Li, H.; Yager, K. G.; Starr, F. W.; Tkachenko, A. V.; Gang, O. Diamond family of nanoparticle superlattices. *Science* **2016**, *351*, 582–586.
- (16) Huang, M.; Hsu, C. H.; Wang, J.; Mei, S.; Dong, X.; Li, Y.; Li, M.; Liu, H.; Zhang, W.; Aida, T.; Zhang, W. B.; Yue, K.; Cheng, S. Z. Selective assemblies of giant tetrahedra via precisely controlled positional interactions. *Science* **2015**, *348*, 424–428.
- (17) Ye, X.; Collins, J. E.; Kang, Y.; Chen, J.; Chen, D. T.; Yodh, A. G.; Murray, C. B. Morphologically controlled synthesis of colloidal upconversion nanophosphors and their shape-directed self-assembly. *Proc. Natl. Acad. Sci. U.S.A.* **2010**, *107*, 22430–22435.
- (18) Henzie, J.; Grünwald, M.; Widmer-Cooper, A.; Geissler, P. L.; Yang, P. Self-assembly of uniform polyhedral silver nanocrystals into densest packings and exotic superlattices. *Nat. Mater.* **2011**, *11*, 131–137.
- (19) Zhang, J.; Luo, Z.; Quan, Z.; Wang, Y.; Kumbhar, A.; Smilgies, D. M.; Fang, J. Low packing density self-assembled superstructure of octahedral Pt₃Ni nanocrystals. *Nano Lett.* **2011**, *11*, 2912–2918.
- (20) Choi, J. J.; Bian, K.; Baumgardner, W. J.; Smilgies, D. M.; Hanrath, T. Interface-induced nucleation, orientational alignment and symmetry transformations in nanocube superlattices. *Nano Lett.* **2012**, 12, 4791–4798.
- (21) Singh, G.; Chan, H.; Baskin, A.; Gelman, E.; Repnin, N.; Král, P.; Klajn, R. Self-assembly of magnetite nanocubes into helical superstructures. *Science* **2014**, *345*, 1149–1153.
- (22) Lee, Y. H.; Shi, W.; Lee, H. K.; Jiang, R.; Phang, I. Y.; Cui, Y.; Isa, L.; Yang, Y.; Wang, J.; Li, S.; Ling, X. Y. Nanoscale surface chemistry directs the tunable assembly of silver octahedra into three

- two-dimensional plasmonic superlattices. Nat. Commun. 2015, 6, 6990.
- (23) Yu, Y.; Lu, X.; Guillaussier, A.; Voggu, V. R.; Pineros, W.; de la Mata, M.; Arbiol, J.; Smilgies, D. M.; Truskett, T. M.; Korgel, B. A. Orientationally ordered silicon nanocrystal cuboctahedra in superlattices. *Nano Lett.* **2016**, *16*, 7814–7821.
- (24) Lin, H.; Lee, S.; Sun, L.; Spellings, M.; Engel, M.; Glotzer, S. C.; Mirkin, C. A. Clathrate colloidal crystals. *Science* **2017**, *355*, 931–935.
- (25) Gong, J.; Newman, R. S.; Engel, M.; Zhao, M.; Bian, F.; Glotzer, S. C.; Tang, Z. Shape-dependent ordering of gold nanocrystals into large-scale superlattices. *Nat. Commun.* **2017**, 8, 14038.
- (26) Wang, D.; Hermes, M.; Kotni, R.; Wu, Y.; Tasios, N.; Liu, Y.; de Nijs, B.; van der Wee, E. B.; Murray, C. B.; Dijkstra, M.; van Blaaderen, A. Interplay between spherical confinement and particle shape on the self-assembly of rounded cubes. *Nat. Commun.* **2018**, *9*, 2228
- (27) Russo, J.; Romano, F.; Tanaka, H. New metastable form of ice and its role in the homogeneous crystallization of water. *Nat. Mater.* **2014**, *13*, 733–739.
- (28) Frank, F. T.; Kasper, J. Complex alloy structures regarded as sphere packings. I. Definitions and basic principles. *Acta Crystallogr.* **1958**, *11*, 184–190.
- (29) Haji-Akbari, A.; Engel, M.; Keys, A. S.; Zheng, X.; Petschek, R. G.; Palffy-Muhoray, P.; Glotzer, S. C. Disordered, quasicrystalline and crystalline phases of densely packed tetrahedra. *Nature* **2009**, *462*, 773–777.
- (30) Damasceno, P. F.; Engel, M.; Glotzer, S. C. Crystalline assemblies and densest packings of a family of truncated tetrahedra and the role of directional entropic forces. *ACS Nano* **2012**, *6*, 609–614.
- (31) Boles, M. A.; Talapin, D. V. Self-assembly of tetrahedral CdSe nanocrystals: effective "patchiness" via anisotropic steric interaction. *J. Am. Chem. Soc.* **2014**, *136*, 5868–5871.
- (32) Nagaoka, Y.; Tan, R.; Li, R.; Zhu, H.; Eggert, D.; Wu, Y. A.; Liu, Y.; Wang, Z.; Chen, O. Superstructures generated from truncated tetrahedral quantum dots. *Nature* **2018**, *561*, 378–382.
- (33) Nagaoka, Y.; Zhu, H.; Eggert, D.; Chen, O. Single-component quasicrystalline nanocrystal superlattices through flexible polygon tiling rule. *Science* **2018**, *362*, 1396–1400.
- (34) Zheng, Y.; Liu, W.; Lv, T.; Luo, M.; Hu, H.; Lu, P.; Choi, S. I.; Zhang, C.; Tao, J.; Zhu, Y.; Li, Z. Y.; Xia, Y. Seed-mediated synthesis of gold tetrahedra in high purity and with tunable, well-controlled sizes. *Chem.—Asian J.* **2014**, *9*, 2635–2640.
- (35) Wang, Y.; Chen, J.; Zhu, C.; Zhu, B.; Jeong, S.; Yi, Y.; Liu, Y.; Fiadorwu, J.; He, P.; Ye, X. Kinetically controlled self-assembly of binary polymer-grafted nanocrystals into ordered superstructures via solvent vapor annealing. *Nano Lett.* **2021**, *21*, 5053–5059.
- (36) Liu, Y.; Klement, M.; Wang, Y.; Zhong, Y.; Zhu, B.; Chen, J.; Engel, M.; Ye, X. Macromolecular ligand engineering for programmable nanoprism assembly. *J. Am. Chem. Soc.* **2021**, *143*, 16163–16172.
- (37) Walker, D. A.; Leitsch, E. K.; Nap, R. J.; Szleifer, I.; Grzybowski, B. A. Geometric curvature controls the chemical patchiness and self-assembly of nanoparticles. *Nat. Nanotechnol.* **2013**, *8*, 676–681.
- (38) Zheng, P.; Paria, D.; Wang, H.; Li, M.; Barman, I. Optical properties of symmetry-breaking tetrahedral nanoparticles. *Nanoscale* **2020**, *12*, 832–842.
- (39) Avendaño, C.; Escobedo, F. A. Phase behavior of rounded hard-squares. *Soft Matter* **2012**, *8*, 4675–4681.
- (40) van Anders, G.; Ahmed, N. K.; Smith, R.; Engel, M.; Glotzer, S. C. Entropically patchy particles: engineering valence through shape entropy. *ACS Nano* **2014**, *8*, 931–940.
- (41) van Damme, R.; Coli, G. M.; van Roij, R.; Dijkstra, M. Classifying crystals of rounded tetrahedra and determining their order parameters using dimensionality reduction. *ACS Nano* **2020**, *14*, 15144–15153.

- (42) Deegan, R. D.; Bakajin, O.; Dupont, T. F.; Huber, G.; Nagel, S. R.; Witten, T. A. Capillary flow as the cause of ring stains from dried liquid drops. Nature 1997, 389, 827-829.
- (43) Israelachvili, J. N. Intermolecular and Surface Forces, 3rd ed.; Elsevier, 2011; p 516.
- (44) Young, K. L.; Jones, M. R.; Zhang, J.; Macfarlane, R. J.; Esquivel-Sirvent, R.; Nap, R. J.; Wu, J.; Schatz, G. C.; Lee, B.; Mirkin, C. A. Assembly of reconfigurable one-dimensional colloidal superlattices due to a synergy of fundamental nanoscale forces. Proc. Natl. Acad. Sci. U.S.A. 2012, 109, 2240-2245.
- (45) Kim, J.; Song, X.; Ji, F.; Luo, B.; Ice, N. F.; Liu, Q.; Zhang, Q.; Chen, Q. Polymorphic assembly from beveled gold triangular nanoprisms. Nano Lett. 2017, 17, 3270-3275.
- (46) Rupich, S. M.; Shevchenko, E. V.; Bodnarchuk, M. I.; Lee, B.; Talapin, D. V. Size-dependent multiple twinning in nanocrystal superlattices. J. Am. Chem. Soc. 2010, 132, 289-296.
- (47) Bühler, J.; Prior, Y. Study of morphological behavior of single diamond crystals. J. Cryst. Growth 2000, 209, 779-788.
- (48) Angus, J. C.; Sunkara, M.; Sahaida, S. R.; Glass, J. T. Twinning and faceting in early stages of diamond growth by chemical vapor deposition. J. Mater. Res. 1992, 7, 3001-3009.

□ Recommended by ACS

Superlattice Engineering with Chemically Precise Molecular Building Blocks

Xiao-Yun Yan, Stephen Z. D. Cheng, et al.

DECEMBER 16, 2021

JOURNAL OF THE AMERICAN CHEMICAL SOCIETY

READ 2

Macromolecular Ligand Engineering for Programmable Nanoprism Assembly

Yang Liu, Xingchen Ye, et al.

SEPTEMBER 22, 2021

JOURNAL OF THE AMERICAN CHEMICAL SOCIETY

READ 🗹

High-Throughput Preparation of Supramolecular Nanostructures on Metal Surfaces

Jiayi Lu, Qiang Sun, et al.

JULY 21, 2022

ACS NANO

READ **C**

Dictating Nanoparticle Assembly via Systems-Level **Control of Molecular Multivalency**

Peter J. Santos, Robert J. Macfarlane, et al.

AUGUST 29, 2019

JOURNAL OF THE AMERICAN CHEMICAL SOCIETY

READ 2

Get More Suggestions >